Dynamic-energy-budget-driven fruiting-body formation in myxobacteria

M. Hendrata[1,*] and B. Birnir[2]
[1]*Department of Mathematics, California State University, 5151 State University Drive, Los Angeles, California 90032, USA*
[2]*Center for Complex and Nonlinear Science and Department of Mathematics, University of California, Santa Barbara, California 93106, USA*

(Received 15 June 2008; revised manuscript received 11 March 2010; published 1 June 2010)

We develop an interacting particle model to simulate the life cycle of myxobacteria, which consists of two main stages—the swarming stage and the development (fruiting body formation) stage. As experiments have shown that the phase transition from swarming to development stage is triggered by starvation, we incorporate into the simulation a system of ordinary differential equations (ODEs) called the dynamic energy budget, which controls the uptake and use of energy by individuals. This inclusion successfully automates the phase transition in our simulation. Only one parameter, namely, the food density, controls the entire simulation of the life cycle.

DOI: 10.1103/PhysRevE.81.061902 PACS number(s): 87.18.Fx, 87.17.Jj, 87.18.Ed, 87.18.Gh

I. INTRODUCTION

Myxobacteria (*Myxococcus xanthus*) change their life cycle according to food availability in their environment. In an ideal condition, myxobacteria grow as swarms that spread away from the center of a colony to search for nutrients from the medium and oxygen from above. However, when nutrients are depleted, myxobacteria undergo a phase transition in which they stop growing individually, but instead they merge and build a complex structure, called the fruiting body. The stage of fruiting body development is thus initiated by starvation and built by cell movements and interactions. The substages of fruiting body development that are observed in the experiments consist of the formation of traffic jams and initial aggregates, streaming, formation of three-dimensional hemispherical mounds, formation of toroidal mounds, and sporulation within the fruiting body [1].

In addition to starvation condition, there are other two crucial factors required for the cells to proceed through the stages in their life cycle. The first one is the cell motility. Experiments have shown that there are two motility engines in myxobacteria, namely, the social (S) motility and the adventurous (A) motility. Nonmotile cells, which lack both of these motility systems, are unable to form fruiting bodies [2]. S motility is driven by type IV pili that are found on the cell's leading pole [3,4]. The cell can shoot its pili and attach them to other cell or group of cells nearby. When the pili retract, the cell body gets pulled forward toward the group. A motility is driven by slime secretion from the cell's lagging pole. This slime secretion generates thrust that pushes the cell forward [5]. Cells have the tendency to turn at acute angle and follow the slime trails secreted by other cells [6]. A wild-type ($A+S+$) cell possesses both A and S motility engines. The $A+S-$ strain has only the A motility, while the $A-S+$ strain has only the S motility. These three strains exist and can be studied in a laboratory environment [3].

The other factor that is important in fruiting body development is the cell signaling. Among many types of cell signaling that occur during the development, C-signaling is the one that controls the initial aggregation and also the transition between the substages during the fruiting body formation. C-signal is a 17-kDa cell-surface protein that is transmitted by end-to-end contact between two cells [2,7]. Once C-signal molecule is inserted onto the cell surface, the expression of the csgA gene increases and this in return creates a positive feedback loop that increases the number of C-signal molecules on the signaling cells at an exponential rate. As increasing C-signal reaches different levels, it provides the thresholds that trigger the cell to proceed through the substages of the fruiting body development in a proper temporal order [7,8]. The cells within the fruiting body continue to C-signal until their individual C-signal level has reached the final threshold for differentiation into spores.

Several models have been proposed to explain myxobacterial swarming and fruiting body formation. Two continuous models analyze the spreading rates of myxobacteria swarms on both short and long time scales [9]. Alber's group developed two types of discrete models: lattice and off-lattice. Both discrete models are based on nonchemotactic cell-cell interactions. Their early lattice gas cellular automaton (LGCA) model succeeds in modeling the initial aggregation and stream formation and 3D stochastic LGCA model simulates the two stages of cell aggregation [10]. Later on, their unified 3D LGCA model successfully produces all stages of the fruiting body formation [11]. They next developed an off-lattice model to minimize the geometric constraint inherited in the lattice model. Their off-lattice model simulates myxobacterial swarming and quantifies the contributions of A and S motilities to swarming [12,13].

In this paper we extend Alber's off-lattice model by adding cell growth and cell division mechanism and further develop an algorithm to simulate the entire life cycle of myxobacteria, which includes the swarming and the fruiting body development. Our model consists of four main components, namely, the off-lattice cell representation, the motility algorithm, a logistic equation, and a dynamic energy budget (DEB) equations. The off-lattice cell representation and motility algorithm are described in Secs. II and VII, respectively. A logistic equation is an ODE that we use to describe the behavior of C-signal level during the development. DEB is a system of ODEs that describes the acquisition and use of

*mhendra@calstatela.edu

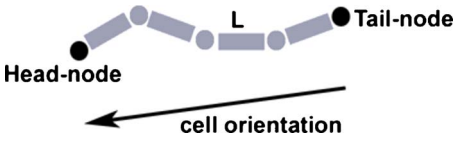

FIG. 1. (Color online) A cell with five nodes, each of which is connected by a segment of length L. The vector indicates its tail-to-head cell orientation. When the cell undergoes a polarity reversal, this tail-to-head cell orientation is reversed.

energy by individuals. The source for this energy is the nutrient uptake and thus it reflects the cell's internal dynamics when nutrient availability is depleted. The DEB and logistic equation are explained in details in Secs. III and IV, respectively. Our simulation shows that the interplay between the logistic equation and the DEB model can automate the phase transition from the swarming to the fruiting body development stage. The internal energy level solved from the DEB equations triggers the phase transition, and the cell's C-signal level solved from the logistic equation controls the switching of the substages of the development. As a result, the simulation of the entire life cycle can be done with only one control parameter, namely, the food (nutrient) density, that is reduced to simulate starvation.

II. OFF-LATTICE MODEL

Similar to the off-lattice model initially introduced in [12,13], a cell is represented by a string of nodes. Even though a myxobacteria cell does not have a physical head and tail, we refer to the leading pole as the *head* node and the lagging pole as the *tail* node (Fig. 1). A vector pointing from tail to head node defines the cell orientation.

Experiments have also shown that cells undergo periodic polarity reversal [14], and this has previously been modeled by Alber's group [15]. We model this polarity reversal by simply reversing the cell orientation and regard the head node as the tail and vice versa. Cell growth is modeled by adding a node, which represents the additional length gained during growth. Cell division mechanism is described in Fig. 2 and it involves splitting the cell in such a way that each daughter cell has length that is equal to half of the parent cells.

In this discrete off-lattice model we assume that cell movement is driven by the head node. This means that the head node determines where the cell will move to. The other nodes then get pulled forward following the head node. In each iteration, cell k updates its head node position according to the discrete model

$$\mathbf{x}_k(t+\Delta t) = \mathbf{x}_k(t) + v\mathbf{V}_k(t)\Delta t + \vec{\epsilon} dB_t^k, \tag{1}$$

where Δt is the time step, $\mathbf{x}_k$ is the vector position of the head node of cell k, $\vec{\epsilon} dB_t^k$ is white noise, v is the constant head velocity, and $\mathbf{V}_k(t)$ is the unit direction due to A and S motilities. A motility is associated with the cell's ability to secrete slime from its lagging pole while moving forward, and at the same time, search for slime trail deposited by other cells that is ahead of it. Once it finds a slime trail, the cell turns at acute angle to follow the trail. The S motility is associated with the ability of cells' pili at the leading pole to shoot and attach the pili to other cells ahead of it and pull the cell body forward when the pili retract. A parameter r_s in our simulation defines the radius of the area within which a cell can search for the slime trail, while a parameter r_p denotes the length of pili of a cell that facilitates S motility. More detailed description of A and S motility algorithm can be found in Sec. VII (methods).

One obstacle in modeling a biological system is that there are too many particles (cells) to simulate. A typical myxobacteria colony consists of at least millions of cells and due to computational complexity, it is almost unreasonable to simulate all of them. Thus, we simulate fewer number of cells and regard each cell in the simulation as a *superindividual*. Each superindividual cell represents a certain number of cells in the actual experiment, all of which behave in an identical manner as a single individual. In doing so, one needs to ensure that the simulation of superindividuals is a valid representation of the simulation of large number of individual cells. We first derive the scaling law associated with Eq. (1) to see how these parameters relate to one another, and next we derive the scaling factor that tells us how we should scale these parameters when we simulate superindividuals instead of individuals.

From Eq. (1), one can deduce a simple relationship

$$\Delta x = v\Delta t + \epsilon^* dB_t, \tag{2}$$

where Δt is the time step, Δx is the distance a cell travels in one time step, ϵ^* is the noise magnitude, and v is the speed of a cell, which is kept constant in our simulation. In our simulation Δt and Δx are the temporal and spatial resolutions, respectively. It follows that Δx, Δt, and ϵ^* scale linearly. In addition, we note that the radius of the slime searching area r_s in the A motility and the length of the pili r_p in the S motility are other parameters that also scale linearly with the spatial resolution. Hence, we arrive at the following linear scaling relationship between various parameters:

$$\Delta t \propto \Delta x \propto \epsilon^* \propto r_s \propto r_p. \tag{3}$$

We now consider a domain of area A, which we divide into small squares, each of which has side equals Δx. Let n be the number of superindividual cells in a square. Then the density of this square is given by $\rho = \frac{n}{\Delta x^2}$. Assuming the density is uniform throughout the entire domain and the number of superindividuals in a square is fixed, then the total number of superindividuals in our simulation is $n_T = \frac{nA}{\Delta x^2}$. If N is the

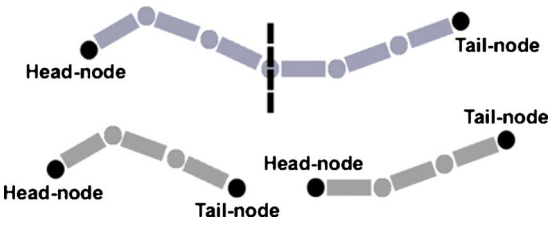

FIG. 2. (Color online) A parent cell divides in the middle into two daughter cells with length half of the parent cell's, mimicking bacterial binary fission.

number of cells in an actual laboratory experiment, then the number of cells each superindividual represents is given by

$$\beta = \frac{N}{n_T} = \frac{N\Delta x^2}{nA}. \tag{4}$$

Thus, simulation of individual cells would give us $\beta=1$. From Eq. (4), it follows that

$$n = \frac{N\Delta x^2}{\beta A}. \tag{5}$$

We keep n constant to ensure the consistency in the dynamics of the simulation. Here, N and A are also constant. If Δx_0 and Δx denote the spatial resolution in the simulation of individuals and superindividuals, respectively, then Eq. (5) gives us the relationship

$$\frac{N\Delta x^2}{\beta A} = \frac{N\Delta x_0^2}{\beta_0 A}.$$

Note that in the simulation of individuals, we have $\beta_0=1$, and therefore

$$\Delta x = \sqrt{\beta}\Delta x_0 = \sqrt{N/n_T}\Delta x_0 \tag{6}$$

and the scaling factor is $\sqrt{N/n_T}$.

III. DYNAMIC ENERGY BUDGET

DEB is the study of the mechanisms of acquisition and use of energy by individuals that has consequences in physiological organization and the dynamics of populations and ecosystems. It is closely related to bioenergetics that focuses on molecular aspects and metabolic pathways in a thermodynamic setting. DEB theory treats individuals as nonlinear dynamics systems. This approach has firm physiological roots and provides a sound basis for population dynamic theories. The aim of the DEB theory is to identify the main rule for the uptake and use of substrates (nutrients, light, and food) that all organism have in common and to develop a simple quantitative framework for metabolism, or respiration, as it changes during the life cycle of an organism, based on elementary physico-chemical principles [16].

DEB is ultimately a scaling theory. It traces its origin to historical studies of metabolic rate measured as rate of oxygen consumption and production of carbon dioxide. Growth of individuals is seen as the difference between build up and breakdown. The process of build up that becomes known as the anabolic process is supposed to be directly proportional to the metabolic process that in turn is supposed to be proportional to surface area. The process of breakdown that is called the catabolic process is supposed to be proportional to volume. Weight is proportional to volume and the growth rate becomes a weighted average between surface area and volume. Thus, organisms that differ considerably in their growth regulating system satisfy the same growth curve known as the von Bertalanffy curve or the solution of the logistic equations with saturated growth. The DEB theory specifies a model for the individual but this model can also be used to model populations and ecosystems in terms of populations. The DEB model for the individual also serves as a constraint for modeling suborganismal processes such as regulations processes that specify details of the physiological behavior of the individual. Thus DEB provides a link across spatial and temporal scales and excludes for example rapid processes at large spatial scales and slow processes at small spatial scales.

We incorporate the following standard DEB model as described in [17]

$$\frac{dL}{dt} = \frac{\dot{\nu}}{3}\frac{([E]/[E_m]) - (L/L_m)}{g + ([E]/[E_m])}, \tag{7}$$

$$\frac{d[E]}{dt} = \frac{\{\dot{A}_m\}}{L}\left(f - \frac{[E]}{[E_m]}\right). \tag{8}$$

The primary parameters in this model are $[E]$=internal energy density (stored energy per cubed length), $[E_m]$ =maximum storage energy, L=cell length ($\propto$ cubic root of structural biovolume), L_m=maximum cell length, $\{\dot{A}_m\}$ =maximum assimilation rate per surface area, and the compound parameters are defined as follows:

$$f = \text{scaled functional response: } \frac{X}{K+X},$$

$$g = \text{investment ratio: } \frac{[G]}{\kappa[E_m]},$$

$$\dot{\nu} = \text{energy conductance: } \frac{\{\dot{A}_m\}}{[E_m]},$$

where the investment ratio is the cost for growth as a fraction of the maximum energy density, and the energy conductance is the maximum energy flux across a surface relative to the maximum energy storage capacity [18]. The other primary parameters are X=food density, K=saturation coefficient, κ =fraction of utilized energy spent on maintenance and growth, and $[G]$=energy costs for a unit increase in size.

In the context of myxobacteria, the "food" in the DEB model above refers to essential amino acids such as leucine, isoleucine, valine, and methionine. These substrate are known to be the essential sources of carbon and energy for myxobacteria during this vegetative growth [19]. Cell growth stops and the cells also immediately stop outward swarming when they sense an amino acid shortage [2,20]. By using the concept of synthesizing unit, the DEB model [Eqs. (7) and (8)] can also be extended to distinguish multiple substrates that correspond to the sources of carbon and energy. However, in this paper we do not make such distinction as one needs to understand the metabolism between nutrients and energy in order to do so and we will investigate this for a future project.

In DEB theory, an individual organism consists of structural biomass and reserves. In DEB model [Eqs. (7) and (8)], they are denoted by L and $[E]$, respectively. Structural biomass is permanent and needs to be maintained continuously, while the reserves function as a continuous supply for maintenance and need not be maintained because they are re-

freshed via assimilation. When the density of the reserves is sufficient, the reserves are also used for the increase in structural biomass, that is, for growth [21].

This standard DEB model assumes all types of nutrients are assimilated into reserves with a rate proportional to the uptake rate. The uptake rate depends on the size of the cell and on the food density. It is also assumed that all assimilation pathways contribute to a single pool of reserves, which then supports all metabolic processes. Energy reserve in the context of DEB theory means a set of metabolites, mostly polymers, that the organism can use for metabolic purposes. These compounds are not just set aside for later use, but they can also be used directly and can have active metabolic functions. Among many compounds in the reserve, one may consider adenosine triphosphate (ATP) and the ribosomal RNA (rRNA) as they play important role as energy supplier and in protein synthesis.

ATP is a complex molecule that is considered as primary energy currency in all organisms. ATP powers all activities of the cell, such as cell growth, locomotion, DNA replication, and cell division (binary fission). The source for constructing the ATP molecule itself is food. However, ATP is not the only main focus in ecoenergetics because ATP itself does not play a leading role in energy fluxes. A typical bacterial cell has approximately 5×10^6 ATP molecules, which is enough for only 2 s of biosynthetic work and the mean lifetime of an ATP molecule is about 0.3 s [16,22,23]. The cell has to make sure that the adenylate energy charge remains fairly constant, which relates to the concept of homeostatis. ATP is part of the machinery used to harvest or mobilize energy [16]. Moreover, cell division cycles and stages in the development of individuals last too long compare to the processes of ATP synthesis and use, which makes the time scales to be irrelevant.

On the other hand, the intracellular concentration of RNA, especially rRNA, increases when the food is abundant. Since ribosomes represent such a large fraction of cellular mass, they are a major storehouse for nutrients. As soon as the food density becomes limiting, RNA degradation begins and the ability of cells to survive during starvation may be related to their capacity to generate nutrients and gain energy from degraded ribosomes [24–27]. RNA plays a key role in balancing the acquisition and utilization of energy in the cell, and its dynamics can be described when it constitutes a fixed fraction of the energy reserve [17,28]. The analysis of the data from [29] also shows that rRNA can be a significant part of the reserves in bacteria. The degradation of RNA leads to the decrease in the internal energy reserves, which is then no longer sufficient to increase the structural biomass. Consequently, cell growth as well as cell division stop during starvation.

We first nondimensionalize the DEB model [Eqs. (7) and (8)] by introducing the scaled cell length $L^*=L/L_m$ and the scaled internal energy density $E^*=[E]/[E_m]$ and obtain the following dimensionless version:

$$\frac{dL^*}{dt}=\frac{\dot{\nu}}{3L_m}\left(\frac{E^*-L^*}{g+E^*}\right), \tag{9}$$

$$\frac{dE^*}{dt}=\frac{\dot{\nu}}{L^*L_m}(f-E^*). \tag{10}$$

Considering the contribution of both ATP and rRNA in the energy reserve, one may also add the following equations into the model

$$E^*=\alpha r^*+(1-\alpha)a^*, \tag{11}$$

$$\frac{da^*}{dt}=0, \tag{12}$$

where r^* and a^* are the scaled level of rRNA and ATP, respectively. The constant α indicates the fixed fraction of the energy reserve consisting of rRNA. In Eq. (12), we set the rate of change of the ATP level to be 0 since the ATP pool of a cell remains steady in the time scale that we use in the model.

From Eqs. (9) and (10), we can see that the decrease in food density X leads to the decrease in $f=X/(X+K)$, which then leads to the decrease in scaled energy reserve E^*. This in turn would reduce dL^*/dt until it eventually becomes 0, which means that the cell stops growing. Here we restrict $dL^*/dt\geq0$ as it makes biological sense that a cell cannot reduce its physical length.

We omit Eqs. (11) and (12) in our simulation to minimize the complexity of the system. Moreover, the use of only one type of reserves will not affect the result as the fruiting body formation is triggered by starvation, which is indicated by the decrease in the reserves below a certain threshold. Thus, the simulation only needs to compute the level of energy reserves of individual cell, given a current food density, to trigger the cell's transition from the swarming stage to the stage of fruiting body development. Hence, the food density is the only parameter that controls the phase transition in the simulation of the life cycle.

From Eqs. (9) and (10) we can derive the threshold in the food density X for starvation condition. We associate starvation condition as a condition where cell growth and cell division stop.

Zusman [30] describes cell division cycle as to consist of the growth phase and division phase. DNA duplication occurs during the growth phase, while division septum formation occurs during division phase. A cell divides after both processes have been completed. For unicellular organism such as bacteria, cell size is the basis of measurement for maturity. Therefore a cell must reach a certain threshold length, say L_a, before it can divide. The level of energy reserve $[E]$ clearly affects the cell's ability to grow and reach the threshold length of L_a and to complete DNA duplication process. Upon reaching the length L_a, the cell then divides after a period of time t_a, which corresponds to the time needed to form the division septum. Data from [30] show that the cells enter the division phase and start forming a division septum at the average length of approximately 4.8 ± 0.11 μm and divide at approximately 5.6 ± 0.21 μm. This sets the parameter values for $L_a\approx4.8$ μm and the length at division $L_d\approx5.6$ μm. Since a myxobacteria cell is known to have a length between 5–7 μm [2], then we can set the scaled length $L_a^*\approx(4.8/7)$ μm$=0.68$ and L_d^*

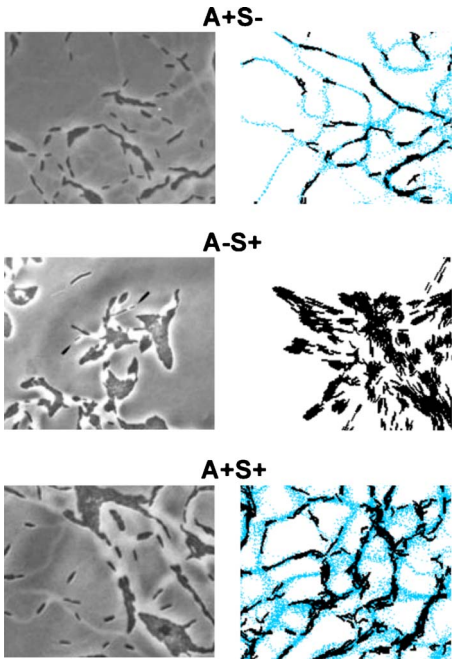

FIG. 3. (Color online) The pattern comparison of $A+S-$, $A-S+$, and $A+S+$ cells during the swarming stage. The left column shows experimental results [5] and the right column shows simulation results based on the A and S motility algorithms and discrete model described in Eq. (1) and Sec. VII, which also includes polarity reversal, cell growth and cell division. The slime trails produced and left by $A+S-$ and $A+S+$ cells are also shown in the simulation (colored in blue/light gray).

$\approx(5.6/7)$ μm=0.8. Then the period of time t_a for the division phase can be found by setting

$$t_a = t(L_d^*) - t(L_a^*), \tag{13}$$

where $t(L_d^*)$ and $t(L_a^*)$ are the time needed to reach the scaled length L_d^* and L_a^*, respectively. Equation (13) also agrees with the definition of the division trigger by [18,31].

Alternatively, the scaled cell length L^* can be defined as the ratio of the cubic root of the actual cell volume W, to that of the maximum cell volume reached by cells that do not divide when living at high food density, that is,

$$L^* = (W/W_m)^{1/3}. \tag{14}$$

We will now derive the expression for $t(L^*)$, the time needed to reach a certain scaled length, and furthermore show mathematically how cell division depends on food density X.

Following [18], we first note that when food density is constant for a sufficiently long time, we have $\frac{dE^*}{dt}=0$ and thus $E^*=f$. Suppose the cell divides at scaled length L_d^*, which by Eq. (14), is defined to be

$$L_d^* = \left(\frac{W_d}{W_m}\right)^{1/3}, \tag{15}$$

where W_d is the cell volume at division. Right after division ($t=0$), the cell volume $W(0)=(1/2)W_d$ due to binary fission. This gives the initial value

$$L^*(0) = \left(\frac{W(0)}{W_m}\right)^{1/3} = 2^{-1/3}L_d^*. \tag{16}$$

Integrating the initial value problem [Eqs. (9) and (16)] yields

$$L^*(t) = f - (f - 2^{-1/3}L_d^*)e^{-\gamma t}, \tag{17}$$

where t is the time since division and

$$\gamma = \frac{\dot{\nu}}{3L_m(g+f)}.$$

Note that as $t\to\infty$ we have $L^*(t)\to f$, which means that the ultimate scaled length when the cell would not divide is equal to f. So for population growth, we must have $L_d^*<f$. Taking the inverse of Eq. (17), it follows easily that

$$t(L^*) = \frac{1}{\gamma}\ln\left(\frac{f - 2^{-1/3}L_d^*}{f - L^*}\right). \tag{18}$$

Substituting Eq. (18) into Eq. (13) gives us

$$f - L_d^* = (f - L_a^*)e^{-\gamma t_a}. \tag{19}$$

Since $L_d^*<f$ for the cell to divide, this forces $f>L_a^*$, and when

$$X \le \frac{L_a^* K}{1 - L_a^*}, \tag{20}$$

the cells are in starvation and they stop growing and dividing.

For simulation purposes, we estimate the values of g and $\dot{\nu}$ as the experimental data for these parameters are unknown. By analyzing the system, one can see that the curves E^* and L^* versus t approach a limiting value that is equal to f. Since a typical doubling time during the swarming stage is about 3 h, we can take this number to be the time period between two consecutive divisions. We set the parameter $f=0.95$, representing the condition for which the nutrient is sufficient, and adjust the parameters $\dot{\nu}$ and g such that the curve L^* versus t falls above L_a^* and is sufficiently close to L_d^* at $t=3$ h. Physically, this ensures that the cell has completed the DNA duplication and reached the threshold length L_a^* for division, and has also obtained an additional growth during the division phase and septum formation, in accordance to experimental data in [30]. We arrive at the estimate $g\approx 0.1$ and $\dot{\nu}\approx 0.15$.

IV. C-SIGNALING

In addition to DEB model [Eqs. (9) and (10)], we also take into consideration the C-signaling that plays important role in changing the cell-cell interaction and coordination, and also in controlling the transition between substages during the fruiting body development. From experiment in [8], it is known that there is on average a few C-signal molecules per cell and this number is increased each time two cells are in pole-to-pole contact. The rate of the increase is exponential and it saturates to its maximum level of several hundred C-signal molecules. This exponential increase and saturation

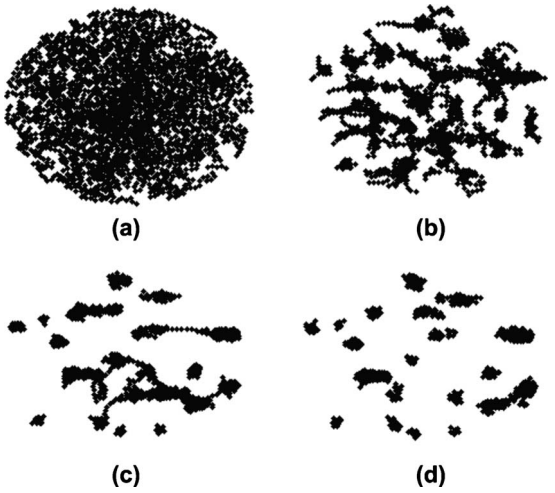

FIG. 4. The formation of aggregates due to deletion of polarity reversal, cell growth and cell division during starvation condition: (a) 400 $A+S+$ cells are randomly placed in circular field; (b) cells stop swarming due to suppression in polarity reversal, cell growth and division, which further results in the change of the global behavior; (c) streams entering an aggregate and joining aggregates are formed as cells no longer reverse; (d) streams disappear and dense stationary aggregates are formed.

are very much similar to the behavior of a logistic equation given by

$$\frac{dN}{dt} = \frac{cN(N_{\max} - N)}{N_{\max}}, \tag{21}$$

where N is the current number of C-signal molecules on the cell surface, $N_{\max}$ is the maximum number of C-signal molecules at the time of sporulation, and c is the logistic constant to be determined.

Furthermore, the increasing level of C-signal modulates the frequency of polarity reversal and also provides different thresholds for triggering different substages in the development. In particular, when a cell has accumulated approximately 25–50 C-signal molecules, it no longer reverses its polarity and that cells start to form aggregates when their C-signal level is approximately 50% of the maximum. Finally, sporulation takes place when their C-signal level has reached the maximum level, in approximately 18 h of development [8,32]. Using these experimental data, we set $N_{\max} \approx 500$ and adjust the logistic constant c such that the graph saturates to $N_{\max}$ in approximately 18 h. We found an estimate of $c \approx 0.002$. We also set several C-signal thresholds: $N_p = 50$ for stopping the polarity reversal, $N_a = 250$ for starting the mound formation, and $N_s = 450$ for sporulation.

V. SIMULATION RESULTS

We run three different simulations, shown in Figs. 3–5, for various purposes. The first one (Fig. 3) is simply a simulation of the swarming stage with no phase transition to fruiting body development. We simulate three different strains of myxobacteria, namely, the $A+S-$, $A-S+$, and $A+S+$ cells, separately during the swarming stage. Our goal here is to

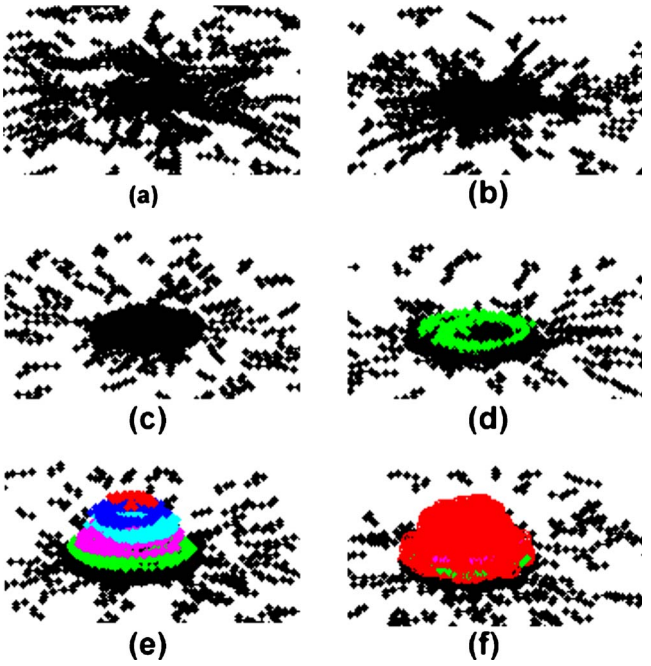

FIG. 5. (Color online) Fruiting body formation stages: (a) initial swarming stage; (b) cells moving in different directions collide and are unable to reverse or turn resulting in the formation of traffic jam; (c) circular motion of incoming cells around the traffic jam causes the aggregate to become round in time; (d) early formation of mound begins when incoming cells start to climb up from the edge of the aggregate to the upper layer (colored in green/light gray). This eventually causes the mound to become hemispherical as the process continues; (e) formation of toroidal mound consisting of five layers (different color indicates different layer); (f) mature fruiting body consisting of nonmotile resistant spores.

justify our motion algorithm given by the discrete Eq. (1) and the A and S motility algorithms described in Sec. VII. Collision between cells is resolved according to collision-handling algorithm, also described in Sec. VII. We do not include DEB and C-signaling (the logistic equation) here as we do not aim to show any phase transitions. However, we include cell's polarity reversal, cell growth, and cell division as they are essential for swarming. We assign two internal clocks for each cell that serves as periodic timer; one to control its polarity reversal and the other to control its growth. The cell divides in the next time period after it has reached the threshold length. Our simulation results exhibit similar patterns as those observed in the experiments, see Fig. 3.

The first row of Fig. 3 shows $A+S-$ cells and the slime trails secreted by each cell. An isolated cell is able to move by itself due to the thrust from slime secretion. We can see many individual cells move freely by themselves following the slime trails. Several cells may come together and form stringy clustering. In contrast, $A-S+$ cells tend to clump and move in groups. An isolated $A-S+$ cell is nonmotile and it can only move when there is another cell or group of cells nearby. The clustering of $A-S+$ cells are shorter, thicker and shaped like arrowheads. The wild-type ($A+S+$) cells exhibit combined patterns of $A-S+$ and $A+S-$ cells. Cell clustering of $A+S+$ is thicker than those of $A+S-$, and it is also longer

than $A-S+$ clusters. There are some cells that move individually, but not as many as in $A+S-$ simulation.

In the second simulation (Fig. 4) we want to show the effect of deletion of polarity reversal, cell growth and cell division on the global behavior of the system. We start with 400 $A+S+$ cells placed randomly in a circular field [Fig. 4(a)]. We assume starvation condition in which each cell can neither grow in length nor divide. In addition, periodic reversal is also turned off. These eliminations prevent the cells to swarm and cause the global behavior of the cells to change during starvation [Fig. 4(b)].

As cells no longer reverse, they follow another cells ahead of it by following the slime trails or by using its pili, and this creates a chain of cells moving together in the same direction without reversing. A chain of many cells moving in the same direction then forms a stream, as observed in experiment [33]. When streaming of cells moving in different directions collide, they stall as they can neither reverse nor turn due to high cell density behind and around them. This results in the formation of traffic jams, which nucleate the aggregate. Streams enter an aggregate and also connect one aggregate to another [Fig. 4(c)]. Through these streams the cells can also be transferred from one aggregate into another. In most cases, smaller aggregates join a larger aggregate. Since we only simulate a limited number of cells, the streams eventually disappear leaving behind denser, stationary aggregation centers that are scattered at random over the field [Fig. 4(d)]. In the experiment, each of these aggregates will develop into a fruiting body. However, in this simulation we do not include DEB and C-signaling, and thus we do not see the transition into fruiting body development here.

Having justified our motility algorithms and the effect of cell growth, division, and polarity reversal in the first two simulations, we now simulate the life cycle of myxobacteria. As fruiting body is a three-dimensional structure, an idealistic goal is to develop a three-dimensional algorithm. However, this would increase the complexity greatly. To avoid this, we extend our simulation into two-dimensional simulation in layers. The advantage of this is that we can accommodate the three-dimensional property of a fruiting body without having to change the motility algorithms we have developed for two-dimensional plane. Each cell in the simulation will have a variable called *layer* indicating in what layer of the fruiting body it is currently located.

We hone in on simulating only one fruiting body to minimize the computational complexity of the system. We initially start with a circular colony consisting of 300 $A+S+$ (superindividual) cells. Since enough number of cells must be present in order to complete a fruiting body and the cells are no longer able to grow and divide during the fruiting body development, we add a certain number of cells from the boundary of the simulation domain periodically so that at the end of the simulation there are approximately 2500 (superindividual) cells. In this simulation, we include the DEB model [Eqs. (9) and (10)] and also the logistic Eq. (21) for C-signaling. Each cell is assigned the following initial values, all of which follow a uniform distribution:

(1) A scaled internal energy E^* between 0 and 1.

(2) A scaled length L^* between 0.5 and 1.

(3) C-signal molecules N between 5 and 10.

(4) Periodic polarity reversal between 6–8 min.

To see how the DEB Eqs. (9) and (10) function as a trigger mechanism from the swarming stage to the stage of fruiting body formation, we first set the food density $X=20$ and the saturation coefficient $K=0.25$. We keep X constant for the first few iterations so that the cells' internal energy E^* can increase, allowing some of them to grow and divide. Cell motion is determined by the A and S motility algorithms, and collision is resolved according to collision-handling algorithm when it occurs. However, when cells are in pole-to-pole contact, Eq. (21) is solved numerically to update the new level of C-signal molecules. Since food density is still relatively high and the cells' C-signal level are still below the threshold $N_p=50$, most cells are in the swarming stage at this point. They move outward away from the center of the colony and periodically reverse their polarity [Fig. 5(a)].

To trigger starvation in the simulation, we decrease X by 5% periodically. This would decrease f and cause E^* to start decreasing as well. When the food density X falls below the threshold given by Eq. (20), the cells are in starvation and they are no longer able to grow as their internal energy E^* falls below a certain threshold. Since division requires a threshold length L_a^*, this also implies that cell division is also prevented by starvation. Thus, the DEB model [Eqs. (9) and (10)] has prevented cell growth and cell division. On the other hand, as cells move, their probability of having pole-to-pole contact is increasing, and thus their level of C-signal also increases. When their C-signal level reaches the threshold N_p, their polarity reversal is switched off. As a result, we see similar behavior as shown in the previous simulation in Fig. 4. When the cells moving in different directions collide, they cannot turn due to high cell density around them. They cannot reverse to resolve collision either as their C-signal level has suppressed polarity reversal. The colliding cells stall and form the traffic jam. This traffic jam nucleates the aggregate. The incoming cells find the aggregate by following the slime trails leading to the aggregate laid down by earlier arriving cells [Fig. 5(b)]. Clearly, this automatic phase transition is triggered by the level of food density and energy density from the DEB model, and also by the level of C-signal from the logistic equation.

Some experiments show that cells in the early stages of fruiting body development often pass through a ripple phase characterized by traveling waves. This phenomenon is due to C-signaling activity and the synchronization of the cells' polarity reversal frequency. When the density of C-signal protein on the cell surface is low, cells respond to collision and C-signaling by reversing their gliding direction. This reversal response to the C-signaling induces the traveling wave patterns characterizing the ripple phase [7,34–36]. The cells control the reversal frequency and their movement becomes periodic. The periodicity of individual cells matches the period of the rippling [20]. However, with each C-signaling event, more C-signal molecules are exported to the cell surface. When the level of C-signal exceeds a threshold, the cells decrease their reversal frequency and move unidirectional in streams [37]. Within streams, cells do not reverse and cells inside the aggregate circulate clockwise and counterclockwise without reversing [38,39].

Our current simulation does not exhibit the rippling phenomenon as we switch off the cells' polarity reversal entirely

whenever the cell's C-signal level has reached threshold N_p. This simplifies the model, however, since our goal is to show that the inclusion of DEB can automate the transition from the swarming to the development stage, the rippling phase that precedes aggregation is a side issue that will not change our simulation result. Traveling waves slightly enhances the C-signaling, but it is not crucial for our simulation purpose and therefore it is omitted.

As the incoming cells hits the traffic jam, the collision-handling algorithm makes them turn or align with the traffic jam. However, their *A* and *S* motility will keep them in contact with the traffic jam as it is the area that has the highest cell density and slime density. As a result, these incoming cells move in the direction circumferential to the boundary of the traffic jam and cause the aggregate to round up [Fig. 5(c)].

Cells continue to C-signal as they move around the aggregate. When the level of C-signal molecules passes the next threshold N_a=250, the cells may start the formation of three-dimensional hemispherical mound. In this stage, some cells leave the base of the aggregate when the cell density is very high. They climb up from the edge of the aggregate to a layer above it [Fig. 5(d)]. As a cell moves up to the upper layer, we increase its *layer* variable by one. The cells in the upper layer continue to move according to *A* and *S* motility and collision algorithms for two-dimensional plane. At the same time the algorithm needs to check that there are cells in the layer underneath it in order to keep the three-dimensional structure physically make sense. As a cell in the upper layer gets closer to the edge of the structure, it turns and follow the circular boundary of the aggregate in the layer below it. Eventually, the cells in the upper layer cover up the traffic jam in the base layer. These cells may also align with one another in the same layer when collision occurs and move together in circular motion. If the cell density in the second layer is high enough, then some cells may move up again from the edge and form the third layer. This process continues until most cells in the simulation domain have formed the mound. Collectively, this upward movement in spiraling fashion, together with cell circular motion in each layer, cause the mound to be hemispherical in time.

The motile cells in the base layer continue to circulate in both clockwise and counterclockwise direction circumferential to the boundary of the aggregate without reversing. The jammed cells on the base layer that are adjacent to these motile cells align their orientations with the orientations of the motile cells and begin to move. This circular movement slowly resolves the traffic jam in the base layer. In the upper layer this circular movement creates a topological singularity that causes the inner part of the fruiting body to have lower density than the outer shell. Eventually, a hole in the middle of the mound starts to form and the hemispherical mound now becomes a fruiting body with hollow center, or sometimes called a toroidal mound [Fig. 5(e)].

Figure 6 shows the internal structure of this toroidal mound with cross sections of the layers. This result agrees with experiment by Sager and Kaiser [40] which shows that the structure of a nascent fruiting body consists of the *inner domain* and the *outer domain*. The hemispherical outer domain is densely packed by cells that move in paths circumferential to the fruiting body perimeter. These cells form clockwise and counterclockwise cell streams in approximately equal proportions and they no longer reverse. In contrast, the inner domain consists of less ordered nonmotile cells at threefold lower cell density.

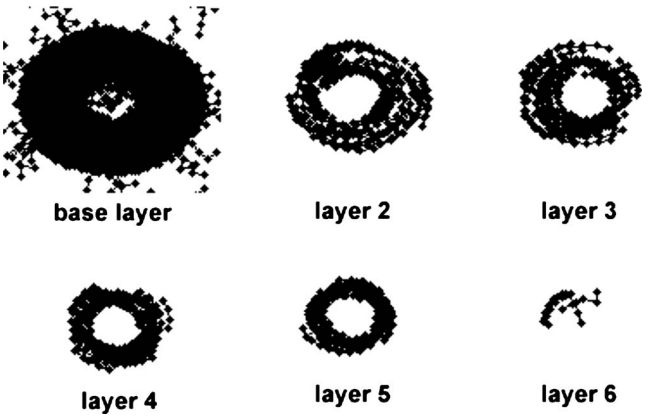

FIG. 6. Cross section of each layer of a nascent fruiting body showing the cells' position and orientation. Darker area corresponds to the outer domain, while lighter area corresponds to the inner domain.

C-signaling continues while cells in the high-density outer domain are moving in circular orbit within the annulus. The level of C-signal molecules on each cell surface increases until it reaches a final threshold of N_s=450 for sporulation. During sporulation, the cell differentiates into spore by shortening and rounding up its rodlike cell body. Figure 7 shows a schematic diagram of the cell differentiation.

Myxospores are unable to move on their own. The cells in the outer domain that differentiate into spores can only be transported passively to the inner domain by undifferentiated motile cells [41]. In our simulation, we model this passive transport as a result of mechanical collisions between the spores and the motile cells, which occurs very likely due to the high density of the outer domain. The details on spore differentiation and spore transport are described in Sec. VII. The transported spores reach the inner domain and fill up the hollow center of the mature fruiting body. Spores that do not get transported into the hollow center stay in the outer domain inside the fruiting body.

With cell sporulation occurring nonstop, all viable cells within the mound eventually differentiate into spores and the fruiting body matures. The spores will be close-packed and fill the entire fruiting body [41]. Figure 5(f) shows a mature fruiting body with close-packed spores fill up the entire structure. The cells outside the fruiting body do not differentiate into spores. Figure 8 shows the cross sections of a ma-

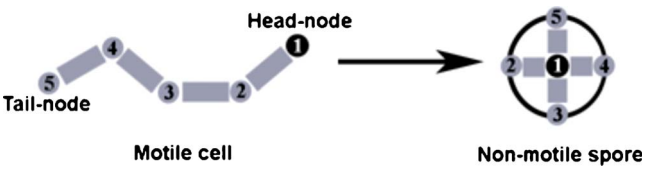

FIG. 7. (Color online) A rod-shaped cell differentiates into a round myxospore.

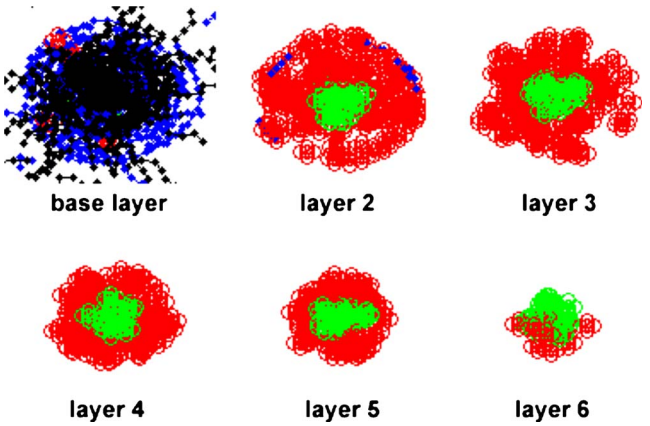

FIG. 8. (Color online) Internal structure of a mature fruiting body consisting of spores. The spores colored in green (light gray) are those that get transported from the outer domain and fill up the middle hole (inner domain) of the fruiting body.

ture fruiting body at each layer. The transported spores are those colored in green (light gray), while those that stay in the outer domain are colored in red (dark gray). The spores fill up the upper layers of the mound, whereas the base layer still contains rod-shaped cells. This result gives a good agreement with the experiment in [42].

VI. DISCUSSION

We develop an off-lattice-based discrete model and the algorithm to produce all stages of myxobacteria life cycle, starting from the swarming stage up to the fruiting body formation, including the sporulation, based on nonchemotactic cell-cell interactions. Our model is basically an interacting particle model for which cell movement is governed entirely by motility algorithms. Thus, it offers transparency and flexibility, which is an advantage in comparison to other off-lattice-based statistical mechanics model that uses Hamiltonian to calculate the probability of accepting new position of the cell. This flexibility allows us to incorporate additional effects related to the biological system that we model, such as the bioenergetics and other environmental factors, which in this paper is the nutrient availability.

In addition to the local rules for cell motility, our model consists of three ODEs. Two ODEs associated with the DEB model keep track of the outer energy (interpreted as the cell length) and the reproductive energy (interpreted as the number of ribosomal RNA). The third ODE is a logistic equation that keeps track of the level of C-signal molecules. The reason why the inclusion of these ODEs automates the simulation of the life cycle is that certain levels of these three quantities initiate the starvation phase (when the cells stop dividing), the formation of the fruiting body (when the cells stop reversing), and finally sporulation (when the level of C-signal molecules reaches its maximum). Once these levels (triggers) are set, the whole simulation of the life cycle is determined by a single parameter, namely, the food density.

It is an interesting problem to let the bacteria deplete the food in an inhomogeneous way. This will create spatial patterns and one can ask how many fruiting bodies are formed given an initial cell density. However, this will be addressed in a separate paper. In this paper we are simply addressing a simpler problem about the "local" formation of a fruiting body and food is all depleted without much spatial structure.

The formation of the fruiting body in our simulation is not controlled in any way; it is simply a global structure formed by the local interaction and the three evolving quantities in the ODEs. The motility in the plane applies if the cells are allowed to go on top of each other and form new two-dimensional layers. We do not use any special algorithm for spore transport. It is simply local interaction and collision between motile cells and spores. The spores are transported into the empty interior of the fruiting body as a result of topology, geometry (the roundness of the spores), and the local interactions.

The scaling formula derived in Sec. II is used to justify the comparison between our simulation of superindividuals and the actual experiments with large number of individual cells. The fruiting body in our simulation consists of 2500 (superindividual) cells. In an actual experiment, a fruiting body consists of approximately 10^5 cells. This implies that each superindividual cell represents approximately 40 single biological cells, all of which behave in identical manner. With the scaling law and the scaling factor, we are now able to analyze how the parameters should scale when we simulate at the level of individual cells, i.e., when we simulate 10^5 cells instead of 2500 superindividuals. We require that the dynamics to remain unchanged when a region is blown up in scale.

In the simulation discussed in this paper, the spatial resolution $\Delta x=10$ μm and the temporal resolution $\Delta t=2$ min. Thus, Eq. (6) will give us

$$\Delta x_0 = \sqrt{n_T/N}\Delta x = \sqrt{2500/10^5}\cdot 10 \ \mu\text{m} \approx 1.6 \ \mu\text{m}$$

and $\Delta t_0=\sqrt{2500/10^5}\cdot 2$ min ≈ 19 s. This gives the actual cell velocity to be approximately 1.6 μm/19 s, which is equivalent to 5.05 μm/min. We note that this is a reasonable number from biological perspective [43]. Thus, by multiplying all related parameters with the correct scaling, we are ensured to get the same dynamics when we simulate at the level of individuals. This also justifies that our simulation result is a good representation of the simulation with large number of individuals.

With our model and its associated scaling law, DEB simulation can now be done to investigate several interesting problems. One is to explore the relationship between population size and its survivability. Myxobacteria colony with various cell density can be simulated and the number of aggregates formed in the domain under starvation or limited and declining food density can be counted. These aggregates may eventually advance into fruiting bodies and sporulate, which allow the colony to survive in unfavorable environment.

Second possible application is derived from the fact that our DEB model uses cell length L and ribosomal RNA (interpreted as a fraction of the internal energy density E) as two measurable entities. One could experimentally verify cell threshold length concept and internal energy density re-

quirement for cell division as proposed in this model. Specifically, knowing the food availability in the domain of a colony of cells, one may predict the growth rate and the behavior of this colony over time by using DEB. So far there is no experimental data found on two problems mentioned above, however, experiments can be done and the results can be compared with the DEB simulations, which we will explore in future publications.

The simulation of the life cycle presented in this paper is done only for $A+S+$ cells. Similar simulation can also be run for $A-S+$ and $A+S-$ cells to further investigate the relationship between lacking one of the motility motors and the delay in fruiting body development as seen in the experiments. Specifically, one can quantitatively measure the difference in the rate at which C-signal level increases between various mutants, which may account for the delay in their fruiting body development.

Lastly, we can also naturally extend the model and use the DEB as a constraint to simulate processes at suborganismal level, such as cell signaling and feeding mechanism. In particular, we are currently working on improving this current model by incorporating the interplay between the quorum sensing A signal and C-signal in coordinating developmental gene expression with cell movements during the early stage of fruiting body formation.

VII. METHODS

In the discrete off-lattice model described in Sec. II, the direction of cell motion is determined by the *A* and *S* motility algorithms in the absence of collision and by collision-handling algorithm otherwise. These algorithms are described below.

A. *A* motility

In our algorithm, two possible factors, namely the cell orientation and the slime orientation, contribute to *A* motility direction. The cell orientation comes into play as the slime secretion from the rear pole of the cell pushes the cell directly forward. We model this motility by trying to orient the cell along its long axis, which is the normalized tail-to-head orientation shown in Fig. 1 and it is given by

$$\mathbf{C}_k = \frac{\mathbf{n}_{k_1} - \mathbf{n}_{k_N}}{\|\mathbf{n}_{k_1} - \mathbf{n}_{k_N}\|}, \tag{22}$$

where $\mathbf{n}_{k_1}$ and $\mathbf{n}_{k_N}$ are the position of the head and tail nodes of cell k, respectively.

As a cell moves forward, it leaves behind trails of polysaccharide slime. In our simulation, we keep track of the cell position by keeping track of the position of each node. Likewise, we keep track of the slime trail by keeping track of the position of the slime points. When a moving cell encounters a slime trail (or slime point), it turns to an acute angle to follow the trail. To model this behavior, we first define the *slime searching circle* to be the circular region around the head node with radius r_s, which we set to be half of the cell length. If there are more than one slime points within the slime searching circle that satisfy the acute angle requirement, then the cell moves toward the slime point which was deposited the latest. This is based on the prediction that the newer slime trails have stronger effect than the older ones. The normalized direction due to slime orientation is given by

$$\mathbf{L}_k = \frac{\mathbf{s} - \mathbf{n}_{k_1}}{\|\mathbf{s} - \mathbf{n}_{k_1}\|}, \quad \text{such that } \mathbf{C}_k \cdot \mathbf{L}_k \geq 0, \tag{23}$$

where $\mathbf{s}$ is the position of the slime point. The inequality in Eq. (23) ensures that the slime point makes an acute angle relative to the tail-to-head orientation of cell k.

Let α_{k_i} and β_{k_i} denote the weights of $\mathbf{C}_k$ and $\mathbf{L}_k$, respectively, at the ith iteration. Since the cell has the tendency to follow the slime trails, the algorithm first searches for the slime points nearby. If it finds at least one slime point within its searching circle that satisfies the angle requirement [Eq. (23)], then we set $\beta_{k_i}=1$. Otherwise $\beta_{k_i}=0$, which corresponds to the situation where there is no slime trail found inside the slime searching circle. In this case, the cell moves according to its tail-to-head orientation with some small random turning angle $\hat{\theta}$. This is based on experimental observation that cells may slightly bend and turn even though there is no slime trail nearby. The formula for the *A*-motility direction is then given by

$$\mathbf{A}_k = \alpha_{k_i}(\mathbf{C}_k + \vec{\epsilon} dB_t^k) + \beta_{k_i}\mathbf{L}_k, \tag{24}$$

with

$$\alpha_{k_i} = \begin{cases} 1 & \text{if } \beta_{k_i} = 0 \\ 0 & \text{if } \beta_{k_i} = 1 \end{cases} \quad \text{and} \quad \vec{\epsilon} dB_t^k = (\cos\hat{\theta}, \sin\hat{\theta}).$$

B. *S* motility

The social interaction arise in *S* motility is mediated by type IV pili that extend from the cell's leading pole and whose length can reach up to one cell length. We first define the *pili interacting area* to be the semicircular region right in front of the head node whose radius r_p is equal to a pilus length. This semicircular region is chosen to account for the known stiffness of the pili which cannot bend too much, and the tendency of the cell to bend or turn to less than 90° angle. If there is a group of cell in this vicinity, then the pili can attach to the group and pull the cell toward it.

We divide the pili interacting area of cell k into two regions: Q1 and Q2, relative to the cell's local coordinate system $X'O'Y'$ as shown in Fig. 9. Each neighboring cell that lies inside this pili interacting area belongs to one of these regions.

Thus, if either Q1 or Q2 is not empty, then the cell moves toward the region whichever one that has the greatest number of cells. The orientations of the neighboring cells in this particular region are then averaged to get the *S* motility direction of cell k

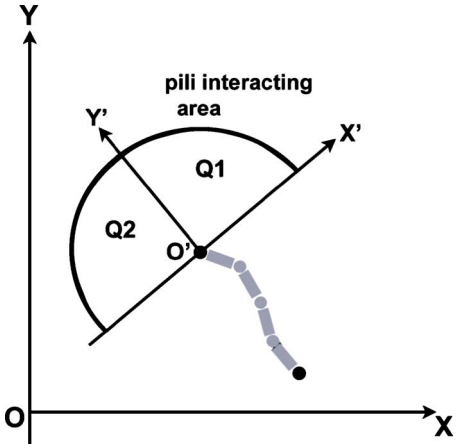

FIG. 9. (Color online) Pili interacting area in S motility algorithm. The pili interacting area represents the vicinity of the pili and its radius can reach up to one cell length.

$$\mathbf{S}_k = \begin{bmatrix} \cos\alpha \\ \sin\alpha \end{bmatrix}, \quad \alpha = \frac{1}{N}\sum_{j=1}^{N} \phi_j, \tag{25}$$

where N is the number of distinct cells in the region to which cell k is moving and ϕ_j is the position angle of cell j in this region with respect to positive X' axis.

C. Discrete equation

In our model we assume that the direction of cell movement is determined by the head node and that a cell moves with a fixed step length L. In each iteration, cell k updates its position according to the discrete Eq. (1), where $\mathbf{V}_k(t)$ is the weighted unit direction due to A and S motility defined by

$$\mathbf{V}_k = \frac{\gamma_k \mathbf{A}_k + \delta_k \mathbf{S}_k}{\|\gamma_k \mathbf{A}_k + \delta_k \mathbf{S}_k\|}. \tag{26}$$

Here γ_k and δ_k are the weights of A and S motility term of cell k. The motility weights for $A-S+$ mutants are taken to be $\gamma_k=0$ and $\delta_k=1$ and vice versa for the $A+S-$ mutants. The wild-type $A+S+$ cells have both A and S motility engines and we assign the weights randomly such that

$$\gamma_{k_i} \in \{0,1\}, \quad \delta_{k_i} = 1 - \gamma_{k_i},$$

where the subscript i refers to the ith iteration.

D. Collision-handling algorithm

In a simulation with high cell density, collision between cells is very likely to occur. We say cell k collides with cell j if the distance between them is less than one cell width. We distinguish two types of collision:

(i) Head-to-body collision: when the head node of cell k collides with a body node of cell j, then cell k randomly chooses to either stall during the current iteration or align to the acute angle with cell j by taking $\mathbf{V}_k = \mathrm{sgn}(\mathbf{C}_k \cdot \mathbf{C}_j)\mathbf{C}_j$, where $\mathbf{C}_j$ is the tail-to-head orientation of cell j as defined in Eq. (22).

(ii) Head-to-head collision: when the head node of cell k collides with the head node of cell j, then $\mathbf{C}_k$ and $\mathbf{C}_j$ are calculated. If the difference in angles between these orientations is close to 180° (head-on collision), then cell k rotates its orientation by some small random angle away from cell j and take the rotated orientation as the new direction $\mathbf{V}_k$. Otherwise, collision is resolved in a way defined in head-to-body collision.

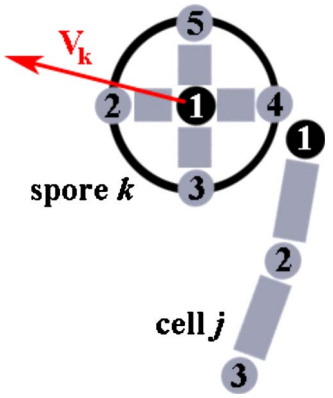

FIG. 10. (Color online) Spore transport mechanism as a result of collision between nonmotile spore and a motile cell.

E. Spore transport algorithm

Spore transport occurs during the final stage of myxobacteria life cycle. Inside a fruiting body, rod-shaped cells that have accumulated enough C-signal molecules differentiate to form a round nonmotile spore. As illustrated in Fig. 7, the head node of the cell becomes the center of the spore and the radius r of the spore k is defined to be half of the length of the segment connecting two consecutive nodes in the initial cell, that is, $r=\frac{1}{2}\|\mathbf{n}_{k_1}-\mathbf{n}_{k_2}\|$, where $\mathbf{n}_{k_1}$ and $\mathbf{n}_{k_2}$ denote the position of the first (head) and second nodes of cell k, respectively.

Spore differentiation does not occur simultaneously during the fruiting body development, and thus mechanical collision between a spore and a nondifferentiated motile cell may occur inside the fruiting body. We say spore k collides with cell j if the distance between the head node of cell j and one of nodes of spore k is less than one cell width. When collision occurs, spore k gets pushed in the direction $\mathbf{V}_k$, the vector pointing from the head node of cell j to the center node of spore k, defined by

$$\mathbf{V}_k = \frac{\mathbf{n}_{k_1} - \mathbf{n}_{j_1}}{\|\mathbf{n}_{k_1} - \mathbf{n}_{j_1}\|},$$

where $\mathbf{n}_{k_1}$ is the center node of spore k and $\mathbf{n}_{j_1}$ is the head node of cell j, as shown in Fig. 10. The center node of spore k will move as far as the spore radius r, and the rest of the nodes of spore k will maintain the distance r from the center node.

Since the cell density in the outer domain of the fruiting body is much higher than the inner domain, many spores that are formed in the outer domain will get pushed in due to collision with other motile cells. They move toward the inner part (inner hole) of the fruiting body and eventually fill up this space, as shown in Fig. 8.

ACKNOWLEDGMENTS

The authors would like to thank Mark Alber (University of Notre Dame, Indiana) and Dale Kaiser (Stanford University, California) for suggestions and helpful discussions.

[1] J. M. Kuner and D. Kaiser, J. Bacteriol. **151**, 458 (1982).
[2] D. Kaiser and R. Welch, J. Bacteriol. **186**, 919 (2004).
[3] D. Kaiser and C. Crosby, Cell Motil. **3**, 227 (1983).
[4] H. Sun, D. R. Zusman, and W. Shi, Curr. Biol. **10**, 1143 (2000).
[5] C. Wolgemuth, E. Hoiczyk, D. Kaiser, and G. Oster, Curr. Biol. **12**, 369 (2002).
[6] R. P. Burchard, J. Bacteriol. **152**, 495 (1982).
[7] S. Kim and D. Kaiser, Proc. Natl. Acad. Sci. U.S.A. **87**, 3635 (1990).
[8] T. M. Gronewold and D. Kaiser, Mol. Microbiol. **40**, 744 (2001).
[9] A. Gallegos, B. Mazzag, and A. Mogilner, Bull. Math. Biol. **68**, 837 (2006).
[10] M. S. Alber, M. A. Kiskowski, and Y. Jiang, Phys. Rev. Lett. **93**, 068102 (2004).
[11] O. Sozinova, Y. Jiang, D. Kaiser, and M. Alber, Proc. Natl. Acad. Sci. U.S.A. **102**, 11308 (2005); **103**, 17255 (2006).
[12] Y. Wu, N. Chen, M. Rissler, Y. Jiang, D. Kaiser, and M. Alber, *Cellular Automata* (Springer-Verlag, Berlin, 2006), p. 192.
[13] Y. Wu, Y. Jiang, D. Kaiser, and M. Alber, PLOS Comput. Biol. **3**, e253 (2007).
[14] D. Kaiser and R. Yu, Curr. Opin. Microbiol. **8**, 216 (2005).
[15] Y. Wu, A. D. Kaiser, Y. Jiang, and M. S. Alber, Proc. Natl. Acad. Sci. U.S.A. **106**, 1222 (2009).
[16] S. A. L. M. Kooijman, *Dynamic Energy and Mass Budgets in Biological Systems* (Cambridge University Press, Cambridge, 2000).
[17] R. M. Nisbet, E. B. Muller, K. Lika, and S. A. L. M. Kooijman, J. Anim. Ecol. **69**, 913 (2000).
[18] S. A. L. M. Kooijman, E. B. Muller, and A. H. Stouthamer, Antonie van Leeuwenhoek **60**, 159 (1991).
[19] A. P. Bretscher and D. Kaiser, J. Bacteriol. **133**, 763 (1978).
[20] R. Welch and D. Kaiser, Proc. Natl. Acad. Sci. U.S.A. **98**, 14907 (2001).
[21] P. P. F. Hanegraaf and E. B. Muller, J. Theor. Biol. **212**, 237 (2001).
[22] F. M. Harold, *The Vital Force: A Study of Bioenergetics* (Freeman, New York, 1986).
[23] A. L. Lehninger, *Bioenergetics* (Benjamin/Cummings, Mnlo Park, CA, 1973).
[24] H. Bremer and P. P. Dennis, in*Escherichia coli and Salmonella*, edited by F. C. Neidhardt (ASM, Washington, 1996), p. 1553.
[25] E. A. Dawes, *The Survival of Vegetative Microbes, 26th Symposium of the Society of General Microbiology*, (Cambridge University Press, Cambridge, 1976), pp. 19–53.,
[26] M. P. Deutscher, J. Biol. Chem. **278**, 45041 (2003).
[27] R. Kaplan and D. Apirion, J. Biol. Chem. **250**, 3174 (1975).
[28] A. L. Koch, J. Theor. Biol. **28**, 203 (1970).
[29] A. A. Esener, J. A. Roels, and N. W. F. Kossen, Biotechnol. Bioeng. **24**, 1445 (1982); **25**, 2803 (1983).
[30] D. Zusman, P. Gottlieb, and E. Rosenberg, J. Bacteriol. **105**, 811 (1971).
[31] W. D. Donachie, Nature (London) **219**, 1077 (1968).
[32] D. Kaiser, Annu. Rev. Microbiol. **58**, 75 (2004).
[33] L. Jelsbak and L. Søgaard-Andersen, Curr. Opin. Microbiol. **3**, 637 (2000).
[34] O. A. Igoshin, A. Mogilner, R. D. Welch, D. Kaiser, and G. Oster, Proc. Natl. Acad. Sci. U.S.A. **98**, 14913 (2001).
[35] O. A. Igoshin, R. Welch, D. Kaiser, and G. Oster, Proc. Natl. Acad. Sci. U.S.A. **101**, 4256 (2004).
[36] L. J. Shimkets and D. Kaiser, J. Bacteriol. **152**, 451 (1982).
[37] L. Jelsbak and L. Søgaard-Andersen, Proc. Natl. Acad. Sci. U.S.A. **96**, 5031 (1999); **99**, 2032 (2002).
[38] B. Julien, D. Kaiser, and A. Garza, Proc. Natl. Acad. Sci. U.S.A. **97**, 9098 (2000).
[39] B. Sager and D. Kaiser, Genes Dev. **7**, 1645 (1993).
[40] B. Sager and D. Kaiser, Proc. Natl. Acad. Sci. U.S.A. **90**, 3690 (1993).
[41] L. J. Shimkets and D. Kaiser, *Cell-cell Signaling in Bacteria* (American Society for Microbiology, Washington, DC, 1999).
[42] R. Lux, Y. Li, A. Lu, and W. Shi, Biofilms **1**, 293 (2004).
[43] D. Kaiser, Nat. Rev. Microbiol. **1**, 45 (2003).